# Role of electronic correlations on the ground-state properties and on the pressure-induced metal-insulator transition in $BaVS_3$

Antonio Sanna, Cesare Franchini, and Sandro Massidda*
*INFM-SLACS, Sardinian Laboratory for Computational Materials Science and Dipartimento di Scienze Fisiche, Università degli Studi di Cagliari, S.P. Monserrato-Sestu km 0.700, I-09124 Monserrato (Cagliari), Italy*

Andrea Gauzzi
*Istituto Materiali per Elettronica e Magnetismo-Consiglio Nazionale delle Ricerche, Area delle Scienze, 43010 Parma, Italy*
(Received 30 April 2004; published 1 December 2004)

We investigated the structural, magnetic and electronic properties of the hexagonal perovskite $BaVS_3$ by means of first-principles calculations within the density functional theory in the local spin density approximation (LSDA) that includes the Hubbard repulsion term $U$ (LSDA+$U$) to take into account electronic correlations. We find that the LSDA+$U$ scheme greatly improves on the LSDA results previously reported, and quantitatively accounts for all ground state properties found experimentally. First, the LSDA+$U$ predicts an orthorhombic structure and a quasi-metallic ground state with a long-range antiferromagnetic (AFM) order in the quasi-hexagonal *ab*-plane, ferromagnetically (FM) coupled along the *c*-axis. Second, we studied the stability of competing crystal structures and competing magnetic orderings in terms of exchange integrals. The results account well for the experimental pressure-dependence of the metal-insulator transition and for the chemical-pressure induced AFM-FM transition reported recently in Sr-substituted samples. In particular, at the experimental value of the volume, $V$, we obtain an energy gap $\Delta=47$ meV, which falls in the range of experimental values (43–59 meV), while, at smaller $V$ values, we find an AFM-FM transition, in agreement with the above effects of Sr-induced chemical pressure. Finally, in the metallic phase, we find a nearly isotropic electrical conductivity, in agreement with experiments, despite the presence of quasi-one-dimensional chains of $VS_6$ along the *c*-axis. We account for such three-dimensional conductivity in terms of the strong interaction between $V$ and $S$ orbitals within each $VS_3$ chain and between adjacent chains.

DOI: 10.1103/PhysRevB.70.235102 PACS number(s): 71.20.−b, 71.30.+h, 71.27.+a, 75.30.Et

## I. INTRODUCTION

3*d*-transition metal (TM) oxides with perovskite-related structure are often characterized by strong correlation effects that lead to a variety of interesting phenomena, such as charge, orbital and magnetic orderings,[1] metal-insulator (MI) transitions[2] and colossal magnetoresistance.[3] These phenomena involve dramatic changes of the electronic and magnetic properties, which constitutes a challenge for our microscopic understanding of strongly correlated electron systems. Recently, research efforts have extended to the field of transition metal sulfides that are less studied. These compounds often display similar structural and electronic properties as compared to oxides. In addition, sulfides offer the opportunity of studying the interplay between electronic correlations and charge instabilities favored by the reduced ionicity of sulfides as compared to oxides.

The object of this work is $BaVS_3$, first synthesized by Gardner, Vlasse, and Wold,[4] that has recently attracted a great deal of interest for its remarkable electronic and magnetic transitions. We should summarize the salient features of this compound that will be recalled throughout this article. $BaVS_3$ possesses the so-called hexagonal perovskite structure, where the sulfur and barium atoms form a closed packed structure in which vanadium atoms occupy the center of face sharing $VS_6$ octahedra aligned in the *c* direction [see Fig. 1(a)]. The intrachain V-V distance of $\approx$2.8 Å along the *c*-axis direction is much shorter than the distance between chains of $\approx$6.7 Å in the *ab*-plane. In spite of this, the physical properties are modestly anisotropic, as indicated by electrical conductivity measurements[5] and previous *ab initio* electronic structure calculations.[6] At $T_s \approx 250$ K,[7,8] the crystal symmetry decreases from hexagonal $P6_3/mmc$ to orthorhombic $Cmc2_1$, owing to a zigzag of the vanadium chains.[9] This structural transition is not associated with any significant change of physical property, although it must be taken into account to determine the ground state properties precisely. Most notable is the metal-insulator (MI) transition at $\approx$70 K accompanied by an AFM-like cusp of the temperature-dependent magnetic susceptibility.[5–28] The latter feature is associated with the opening of a spin gap caused by short-range AFM correlations, thus freezing the spin degrees of freedom.[20] Long range incommensurate AFM order is established in the *ab*-plane only at lower temperature, $T_X \approx 30$ K.[20] Concomitant to the metal-insulator transition, a charge density instability consisting of a charge disproportionation of the vanadium atoms along the *c*-axis appears.[22,26] A further salient feature of $BaVS_3$ is that the AFM interaction is turned into an FM one in sulfur-deficient samples, which leads to a FM long range order with $T_c \approx 15-20$ K.[19,29] Such AFM-FM crossover occurs also under Sr-induced chemical pressure.[11] The crossover indicates that the AFM interaction is weak, although sufficiently strong to prevail over the metallic state below $T_{MI}$. Finally, we should recall the effects of pressure on the above properties. It has been shown[12,16,25] that hydrostatic pressure stabi-

 

lizes the metallic phase and that $T_{MI}$ vanishes at about 2 GPa. To stabilize the effects of external pressure, some of us[11] studied the effects of a partial substitution of the Ba cation with the isovalent and smaller Sr cation. As expected, they observed a substantial compression of the unit cell and the reduction of $T_x$ with increasing chemical pressure. They also observed the appearance of an FM ordering at $\approx$0.10% Sr concentration and an increase of $T_c$ up to 20 K with increasing concentration.

In order to elucidate the microscopic origin of the above electronic and magnetic phase transitions, in this work we perform a detailed *ab initio* electronic structure calculation that properly takes into account the electronic correlations. We focus on the ground state properties and on the pressure-induced changes of these properties. Our calculations are performed within the density functional theory in the local spin density approximation (LSDA) and including the Hubbard repulsion term $U$ within the LSD+$U$ approximation; they are complemented by a structural relaxation study through total energy minimizations. The results are compared with available experiments. The paper is organized as follows. In Sec. II, we describe in detail the computational method. In Sec. III, we illustrate the features of the crystal and magnetic structures studied and additional computational details specific for studying these structures. In Sec. IV, we recall the basic formalism and theoretical framework adopted to calculate the exchange integrals. In Sec. V, we present and discuss the results. Finally, in Sec. VI, we draw the conclusions.

## II. METHOD AND COMPUTATIONAL DETAILS

Our first principles calculations were performed using the VASP (Vienna *ab initio* simulation package) program[30] within the local spin density approximation (LSDA) to the density functional theory (DFT) in the Perdew-Zunger (Ceperly-Alder)[31] parametrization scheme. Conventional LSDA is known to be inadequate to account for the electronic structure of materials with partially filled $d$ or $f$ valence states. Indeed, the only two existing first-principle studies on $BaVS_3$,[6,28] performed using a standard DFT-LSDA approach, predict a metallic ground state instead of the insulating one found experimentally. It is therefore necessary to use more sophisticated approaches[32] that properly take into account on-site Coulomb repulsion. In this work we use the LSDA+$U$ (Ref. 33) approach implemented following the simplified scheme of Dudarev[34] in which the parameters $U$ and $J$ do not enter separately, and only the difference $U-J$ is meaningful. To the best of our knowledge, unfortunately, there are neither spectroscopical nor calculated data available in literature regarding the value of $U$ and $J$ for V in $BaVS_3$ or similar compounds. In the absence of a better alternative we choose $U=4.5$ eV and $J=0.5$, as interpolated in Ref. 35 (where, however, a different many-body scheme was used) and, also, as obtained from an extrapolation of data given in Ref. 36.

Our calculations were carried out within the projector-augmented wave (PAW) method[37] as implemented by Kresse and Joubert.[38] This is a frozen core method which uses the exact valence wave functions instead of nodeless pseudo-wave functions, as commonly done for pseudopotentials calculations. This improves the transferability and reliability of the potentials. We used the following valence electron configurations $5s^2 5p^6 6s^2$, $4s^2 3d^3$, and $3s^2 3p^4$ for the Ba, V, and S, respectively. To determine the plane wave basis set we used a kinetic energy cutoff of about 260 eV, which turned out to give accurate results. To relax atomic positions, we used the interatomic forces calculated by the Hellmann–Feynmann theorem and the geometry was optimized until the change in the total energy was smaller than $10^{-3}$ eV between two consecutive ionic configurations. A $10\times10\times10$ Monkhorst–Pack (MP) type $k$-point mesh, resulting in 125 irreducible $k$-points, was used in all calculations. To improve $k$-point sampling convergence, a Gaussian smearing with an electronic temperature of 0.2 eV was used to find the equilibrium geometry and the density of states (DOS) was computed using the tetrahedron method. We used a supercell geometry (see below) to describe the different magnetic orderings and defects.

## III. CRYSTAL AND MAGNETIC STRUCTURE

The primitive cell of $BaVS_3$ contains two formula units (f.u.) [see Fig. 1(a)], where the vanadium and barium atoms are plotted as spheres of different sizes and sulfur atoms are located at the corners of the black octahedron. The projection of the cell in the *ab*-plane is drawn in the Fig. 1(b) panel as a filled rhomb. The empty rectangle represents the base of the 4 f.u. supercell used in our calculations. It is obtained by doubling the primitive cell on the *ab*-plane. The direction of the vanadium zigzag that drives the structural phase transition at 250 K is marked with double pointed arrows. The calculations were performed mainly using the orthorhombic structure, as the latter was found to be energetically favored than the hexagonal one. The total energy of the latter was calculated by setting the zigzag displacement (intended as the planar shift of the V atoms with respect to the chain axis) to zero and by keeping the $b/a$ ratio fixed and equal to $\sqrt{3}$, in agreement with the experimental structural analysis below 250 K.

Charge density contour plots displaying the difference between the hexagonal and orthorhombic structure caused by the zigzag are shown in Fig. 2. The zigzag creates two inequivalent S sites labeled as S1 and S2, distinguished in Fig. 1 with filled and empty circles, respectivley. The former S1 is located outside the zigzag plane of the V atoms (indicated as *yz* plane in Fig. 2) and roughly maintains the same distance ($\sim$2.38 Å) from the V atoms. The S2 sites lay on the zigzag plane and have, respectively, shorter ($\approx$2.20 Å) and longer ($\approx$2.62 Å) distances from the nearest and second nearest V atoms. From x-ray diffraction data,[8] it was established that the hexagonal symmetry arises from a dynamical effect. Thus, a direct comparison with the experiment would not be appropriate for this symmetry. In addition, the orthorhombic structure turns out to be the most stable one, as shown below.

A supercell approach has been used to study the AFM order in the *ab* plane found experimentally.[20] The supercell

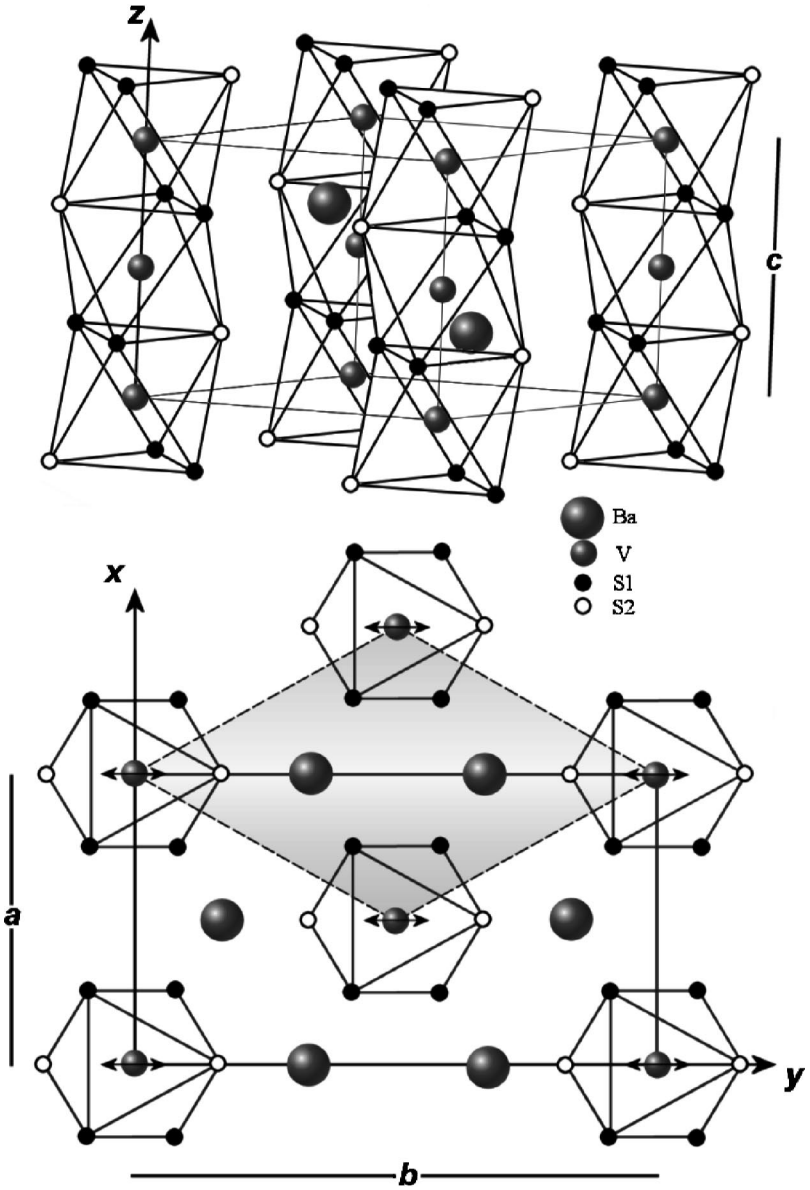


FIG. 1. The primitive cell of $BaVS_3$: (a) tridimensional view for 2 f.u., (b) the base for the 2 f.u. (gray area) and 4 f.u. (rectangular area). We describe both the orthorhombic and hexagonal cells with the Bravais parameters *a*, *b*, *c* as shown in this figure. V atoms are plotted as small gray spheres, barium atoms as big ones, while S1 and S2 atoms are displayed with filled and empty circles, respectively (the difference between S1 and S2 is described in the text). In (b), double pointed arrows mark the V vibration direction which produces the zigzag along the V-V chain.

(see Fig. 1), contains 4 V atoms and allows to describe various competing magnetic orderings. Among them, we studied the FM ordering and the three different kinds of AFM ones shown in Fig. 3 and labeled as AFM-A, AFM-C, and AFM-G. The limitation of our calculations is that the effects of disorder is not taken into account. However, no clear experimental indications exist about the degree of disorder in the crystal and magnetic structures. In addition, structural properties are mainly affected by the local environment rather than by long range order.

## IV. EXCHANGE INTEGRALS

To get an insight into the complex magnetic phase diagram of $BaVS_3$ summarized in the introduction, we evaluated the exchange integrals using the classic Heisenberg spin Hamiltonian,

$$H_{ex} = -\sum_{i,j} J_{i,j} \mathbf{S_i} \cdot \mathbf{S_j}, \tag{1}$$

where the sum is extended over $i,j$ (i.e., each pair appears twice). $J>0$ and $J<0$ for, respectively, FM and AFM exchange and $S=\frac{1}{2}$ is the spin of the $V^{4+}$ atoms characterized by a $3d^1$ electronic configuration. The values of the exchange parameters are obtained by computing the difference of total energy among various magnetic orderings. The number of orderings is determined by the number of exchange constants in Eq. (1). We limit ourselves to nearest neighbor (NN) $J_1$ and second-nearest neighbor (SNN) $J_2$ interactions for the three different antiferromagnetic orderings of Fig. 3 and for the ferromagnetic (FM) ordering. In the orthorhombic phase, we obtain the following expressions:

$$J_1 = \frac{1}{4S^2}(E^A_{\mathrm{AFM}} - E_{\mathrm{FM}}), \tag{2}$$

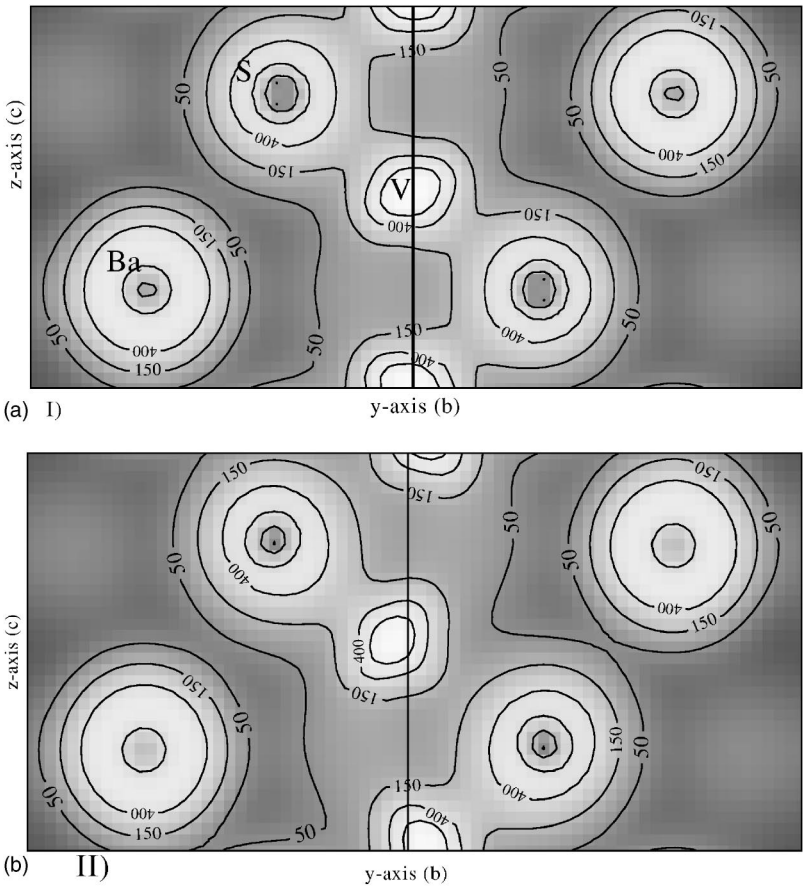


FIG. 2. Contour plot of the valence charge density along the (100) direction cutting a V-V chain. The V atoms are the small circles along the vertical line. In the hexagonal structure (I) the V atoms are aligned along the *z*-direction. In the orthorhombic structure (II), a zigzag causes a S-V dimerization.

$$J_2 = \frac{1}{8S^2}(E^C_{\mathrm{AFM}} - E_{\mathrm{FM}}). \tag{3}$$

In which $J_1$ and $J_2$ refer to the interaction between the two NN V along the *c* direction and the four in-plane SNN V, respectively.

From the knowledge of $J_1$ and $J_2$, the Néel transition temperatures ($T_N$) can be evaluated from the molecular field theory,[39] as follows:

$$T^{\mathrm{AFM\text{-}C}}_{\mathrm{Néel}} = \frac{2S(S+1)}{3k_B}(2J_1 - 4J_2), \tag{4}$$

$$T^{\mathrm{AFM\text{-}A}}_{\mathrm{Néel}} = \frac{2S(S+1)}{3k_B}(-2J_1 + 4J_2), \tag{5}$$

$$T^{\mathrm{AFM\text{-}G}}_{\mathrm{Néel}} = \frac{2S(S+1)}{3k_B}(-2J_1 - 4J_2). \tag{6}$$

## V. RESULTS AND DISCUSSION

In Sec. V A we present the results obtained for the ambient pressure structure, while in Sec. V B, we focus on the pressure-induced modifications of the structural, electronic and magnetic properties.

### A. Ground state properties

We started our calculations by fully minimizing the total energy as a function of the lattice constants for all structural (orthorhombic and hexagonal) and magnetic (FM, AMF-C and AFM-A) phases within the LSDA+$U$ approximation. We also performed a LSDA paramagnetic calculation to investigate the limitations of this simple approximation. The results are summarized in Table I. One notes that the LSDA+$U$ calculated volumes are slightly smaller than the experimental ones by ≈3% and 2% for the hexagonal and orthorhombic phases, respectively. The LSDA values are somehow smaller (≈6%), which is not surprising. The calculated $a$ parameter is smaller by about ≈2%, while the $b$ parameter is larger by ≈1% than the experimental param-

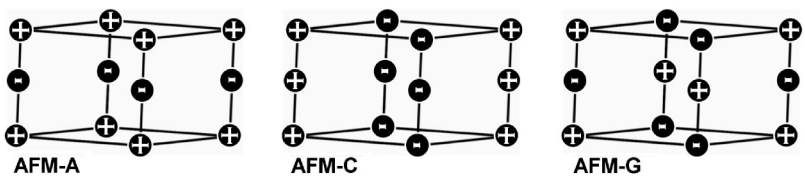


FIG. 3. The figures shows the three different antiferromagnetic structures used in our calculations. The cells schematically refer to the crystal structure of Fig. 1.

TABLE I. Summary of calculated and experimental ($T=5$ K) (Ref. 8) lattice constants. Calculated values are obtained within the LSDA and LSDA+$U$ approximations for both hexagonal ($H$) and orthorhombic ($O$) phases. All values are in Å.

| | | | LSD+$U$ | | | | |
|---|---|---|---|---|---|---|---|
| | | LSD PM | FM | AFM-A | AFM-C | AFM-G | Expt. |
| | $a$ | 6.61 | 6.72 | 6.74 | 6.72 | 6.72 | 6.77 |
| $O$ | $b$ | 11.32 | 11.24 | 11.22 | 11.24 | 11.22 | 11.46 |
| | $c$ | 5.45 | 5.63 | 5.62 | 5.63 | 5.62 | 5.59 |
| $H$ | $a$ | 6.61 | 6.57 | 6.64 | 6.59 | | 6.72 |
| | $c$ | 5.40 | 5.72 | 5.55 | 5.65 | | 5.61 |

eters, which are almost the same in the orthorhombic and hexagonal phases. As to the effect of magnetic ordering on the lattice parameters, in the orthorhombic phase different orderings do not lead to any significant effect. This contrasts with the case of the hexagonal phase, where a ferromagnetic order of the vanadium atoms along the $c$-axis in the FM and AFM-C magnetic structures favors a larger $c$-parameter and, consequently, a shortening of the $a$ and $b$ parameters.

The LSDA+$U$ energies of the different structural and magnetic phases are reported in Table II. One notes that, for all types of magnetic orderings, the orthorhombic phase is favored against the hexagonal one, in agreement with experiments. Thus, in the following we discuss only the results for the orthorhombic phase. The more stable magnetic phase turns out to be the AFM ordering labeled as AFM-C. This phase is almost degenerate with the FM ordering, the energy difference being only 2 meV. This finding perfectly accounts for the experimental scenario below $T_X \approx 30$ K. Indeed, both orderings, AFM-C and FM, are ferromagnetically ordered along the V-V chains (see Fig. 3) and we recall that, in this temperature region, a crossover from in-plane AFM to FM order is induced by sulfur deficiency or chemical pressure.

The other two magnetic structures, namely AFM-G and AFM-A, both having an AFM order along the $c$-axis, are energetically less favored than the previous ones by more than 15 meV. Therefore, we conclude that the FM interaction along the V-V chains is the dominant driving force of the magnetic ground state, independent of the in-plane exchange interaction.

The exchange parameters $J_1$ and $J_2$ evaluated from Eqs. (2) and (3) using the above energies are 12.0 meV and −1.1 meV, respectively. We notice that $J_1$ is positive and one order of magnitude larger than $J_2$, hence its contribution to the Néel temperatures, estimated from 4–6, dominates. The strength of the $c$-axis FM correlation therefore limits the number of energetically favorable magnetic orderings and accounts for the unphysical negative $T_N$ obtained for the AFM-A ($T_N=-165$ K) and AFM-G phases ($T_N=-114$ K) having in-plane AFM ordering. The small $J_2$ obtained can be ascribed to the large distance between two SNN V atoms, ≈6.7 Å (i.e., the interchains distance), and to the absence of anions mediated superexchange paths of the type V-S-V. On the other hand, the distance between two NN V, corresponding to $J_1$, is about 2.8 Å, i.e., more than two times smaller than the SNN distance. The Néel temperature of the AFM-C phase, $T_N=165$ K, is to be compared to the temperature $T\approx 70$ K at which incipient AFM fluctuations appears experimentally. As pointed out in the introduction, the stabilization of a short range in-plane AFM occurs at lower temperature, $T_x \approx 30$ K. The nature of the magnetic interactions occuring in the range 30-70 K, a central issue of debates which clearly deserves further research, is beyond the scope of the present work, and more sophisticated computational tools would be necessary. Taking into account the obvious limitations of the computational method used, the above conclusion is only qualitatively reliable. The quantitative discrepancy between calculated and experimental values for the characteristic energy of AFM correlations is compatible with the following limitations of our approach: (a) the use of molecular field theory is usually affected by significant errors [≈50% (Ref. 39)]; (b) the LDA+$U$ approach is an approximation limited by the uncertainty in the choice of $U$, among other factors, and a rigorous *ab initio* computational method to treat strong electronic correlations is not available yet; (c) the total energy differences involved are in the intrinsic limit of the computational accuracy, thus preventing a precise quantitative estimation of $T_N$.

TABLE II. Total energies of $BaVS_3$ calculated using the LSDA+$U$ approximation for both hexagonal ($H$) and orthorhombic ($O$) phases. Energies are in eV per f.u.

| | FM | AFM-C | AFM-A | AFM-G |
|---|---|---|---|---|
| $O$ | −29.44775 | −29.45000 | −29.43575 | −29.43232 |
| $H$ | −29.34975 | −29.40800 | −29.39525 | −29.39100 |

In Eqs. (2) and (3) $J_1$ and $J_2$ were derived from the FM, AFM-A, and AFM-C total energies. To verify the reliability of these energies, one can use the AFM-G structure as well, thus obtaining a different set of equations for the exchange coupling constants that must lead to nearly the same values of $J_1$ and $J_2$. By doing this, we obtain $J_1=17.2$ meV and $J_2=1.8$ meV, which are significantly different from the

TABLE III. (A) Relevant parameters of the experimental structure at 5 K (Ref. 9) and of the calculated AFM-C structure. The notation $d_{av}$ indicates average distance, $d_{zigzag}$ is the lateral zigzag of the V-V chains. Distances are expressed in Å. (B) Insulating gap ($\Delta$, in meV) for the AFM-C orthorhombic phase of $BaVS_3$ calculated for the equilibrium ($\{abc\}_{th}$) and experimental ($\{abc\}_{expt}$) lattice parameters.

| | Theory | Experiment |
|---|---|---|
| | (A) Geometry | |
| $d$(V-V) | 2.856 | 2.842(28) |
| $d_{av}$(V—S) | 2.387 | 2.386(20) |
| $d_{av}$(Ba—S) | 3.314 | 3.378(26) |
| $d_{av}$ (S-S) | 3.290 | 3.377(8) |
| $d_{zigzag}$(V-V) | 0.24 | 0.25(1) |
| | (B) $\Delta$ | |
| $\Delta$ $\{abc\}_{th}$ | −12.0 | |
| $\Delta$ $\{abc\}_{expt}$ | 47.0 | 43 (Ref. 12)–59(18) (Ref. 25) |

above estimation, for $J_1$ is larger by ≈40% and $J_2$ becomes positive. However, this is only apparently an inconsistency of the calculations. Indeed, in order to obtain fully consistent results for $J_1$ and $J_2$ using the two different sets of structures, one should keep the geometrical parameters (both $a$, $b$, $c$, and internal atomic positions) fixed. This is specifically true for the small energy differences involved. We also notice, furthermore, that both sets of values of $J_1$ and $J_2$ leads exactly to the same Néel temperature for the only stable AFM phase (AFM-C), namely 165 K. The change of sign of $J_2$ and the small change of its absolute value are consistent with the experimental observation of possible spin fluctations[20] indicating a spin-liquid-like state localized in the $ab$-plane, while the $c$-axis ordering is always FM.

We now discuss the structural and electronic properties of the AFM-C orthorhombic phase. In particular, we show that the main experimental features are well explained by our calculations. A comparison between the experimental[9] and calculated atomic positions is given in Table III. The agreement is within the experimental error for the V-V bond length, for the V-V zigzag displacement and for the average S-V distance. On the other hand, the calculated Ba-S and S-S distances are underestimated by about 2%. Similarly to the case of the lattice parameters, the magnetic ordering is not sensitive to the variations of atomic positions. This statement does not apply to the structural changes associated with the metal-insulator transition, as small changes in the interatomic distances are known to greatly affect the Mott transition. We must therefore take these small changes into account to study the effects of pressure on the ground state. We anticipate that, for example, the V-V zigzag displacement and the V—S distance play an important role in the metal-insulator transition, as discussed in Sec. V B.

In Fig. 5 we report the total and V-resolved DOS for the AFM-C phase within the LSDA and LSDA+$U$ approximations. In the former case, the V spin down bands produce a narrow peak around the Fermi level ($E_F$), and the spin up and spin down V peaks are separated by only ≈0.5 eV. Therefore, LSDA fails to reproduce the insulating ground state, which is not surprising. The correlation introduced by means of the $U$-term enlarges the separation between the spin up and spin down peaks of V up to 1 eV and leads to an almost complete depletion of density of states at $E_F$. No gap opens by using the calculated equilibrium atomic positions, at odds with experiments. In Table III we report the gap values for different sets of lattice constants. For the AFM-C structure a negative gap value is found, contrary to the experiments. However, using the experimental volume ($V_{expt}$) obtained by expanding isotropically the calculated lattice parameters $a$, $b$, and $c$, $(abc)_{expt}$, an insulating state with a calculated gap of 47 meV is obtained, in good agreement with the experimental value, $\Delta$=43 (Ref. 12) and 59(18) (Ref. 17) meV. We conclude that the error made in predicting a quasimetallic state at the calculated equilibrium volume ($V_{th}$) can be ascribed to the underestimation of $V_{expt}$ done by LSDA+$U$ and to the failure of LSDA+$U$ to predict the correct $b$-axis value. We see that a 2% discrepancy in the lattice parameters is sufficient to change the nature of the system from insulating to metallic and its strong pressure dependence (Sec. V B).

A further comparison between LSDA and LSDA+$U$ results shows that, as expected, the introduction of the Coulomb term $U$ increases the magnetic moment at the V site from $0.37\mu_B$ to $1.30\mu_B$. The latter value agrees with the experimental values $1.33\mu_B$ (Ref. 12) and $1.15\mu_B$,[10] which further supports the reliability of the LSDA+$U$ approximation. Interestingly, the LSDA+$U$ calculation also leads to a small magnetic moment at the sulfur S1 and S2 sites of $0.06\mu_B$ and $0.09\mu_B$, respectively. This result is not found within the simpler LSDA and is compatible with a strong covalent bond between V and S atoms, that would lead to an incomplete filling of the 3$p$ shell in S.

We now discuss the nature of the bonds based on the band structure (see Fig. 4) and the corresponding total, atomic $l$-decomposed and $lm$-decomposed V and S DOS (see Figs. 5 and 6). In the band plot, thick and thin lines refer to states localized on the S and V sites, respectively. The contribution of Ba is negligible in the energy range considered here. The projection of the states over the atomic orbitals shows that there is a clear distinction between the two groups of occupied and empty bands. These two groups of bands possess a dominant (more than 60% of the states) S and V character, respectively, thus the hybridization between V 3$d$ and S 3$p$ states is not strong. There are only two bands (labeled as $A$ and $B$) crossing $E_F$ near $\Gamma$ and overlapping near $E_F$ with the very small negative gap (−12 meV) mentioned above. The free-electron-like dispersion of these two bands along $\Gamma$-$Z$, $\Gamma$-$Y$, and $\Gamma$-$X$ is nearly equal, about 0.7 eV, which suggests an isotropic conduction in three dimensions. This result is confirmed by the pronounced isotropy of the plasma frequency displayed in the left panel of Fig. 7. Only minor differences are observed between the in- ($xx$ and $yy$) and out- ($zz$) of-plane components. To investigate the nature of the $A$ and $B$ bands, in Fig. 6 we plot the $l$- and $m$-projection of the atom-resolved DOS for the V (a) and S (b) atoms. The

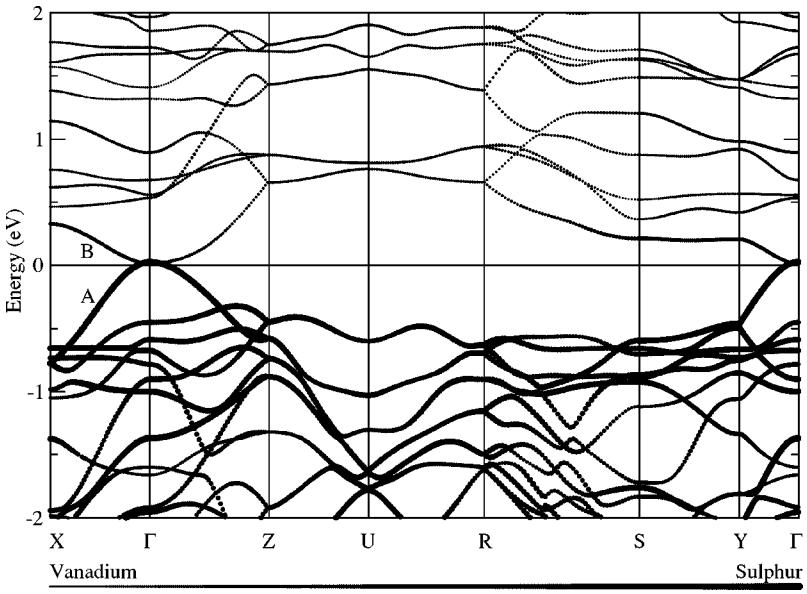


FIG. 4. Band structure near the Fermi level calculated for the orthorhombic AFM-C system. Thick and thin lines indicate states localized at the site of vanadium and sulfur, respectively. *A* and *B* mark the two bands relevant to the MI transition.

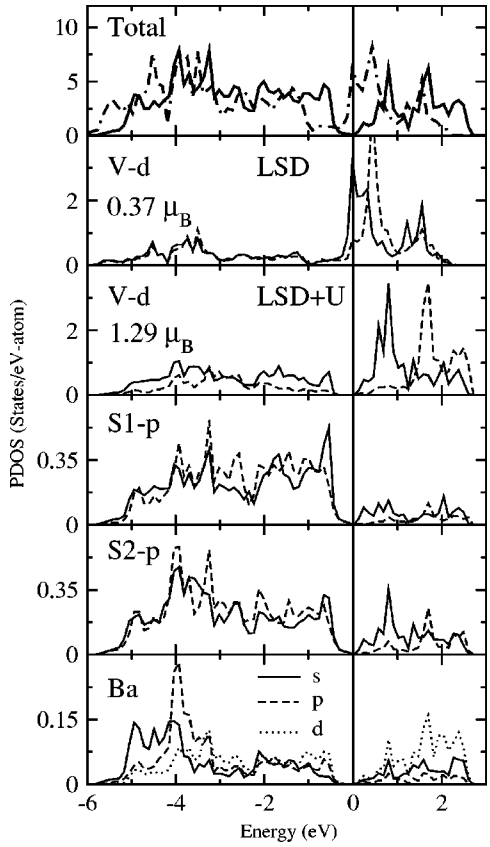


FIG. 5. Total (TDOS) and *l*-decomposed atom resolved (LDOS) density of states of the AFM-C orthorhombic phase calculated within the LSDA+*U* approximation. A comparison with LSDA DOS is given for V and for TDOS (point-dotted line). For V and S atoms we distinguish between spin up (full line) and spin down (dashed line), while for Ba full, dashed, and dotted lines represent *s*, *p*, and *d* states, respectively. The difference between S1 and S2 sites is described in the text. For the V atoms, the corresponding magnetic moments in Bohr units are indicated.

*m*-projected LDOS was calculated with respect to the orthorhombic V lattice quantization axes. The S1 and S2 sites display almost the same $p_y$ and $p_z$ DOS, therefore only the S1 densities are shown. The $p_x$ states are shown separately for S1 and S2, as they are different. Despite the overlap in energy of the V *d* and S *p* bands, the calculated V-DOS in the occupied region is rather small in comparison to the conduction DOS, which confirms the previous conclusion about the V—S hybridization. The only V-states having a significant orbital weight below $E_F$ are the $e_g$ states and especially the $d_{x^2-y^2}\sigma$ orbitals that contribute to the $p\,d\sigma$ V—S bonding. It is noted that the V—S hybridization ensures the three-dimensional conduction character to this material. We infer that the system would otherwise be insulating, since the contribution of states with small V—S hybridization is negli-

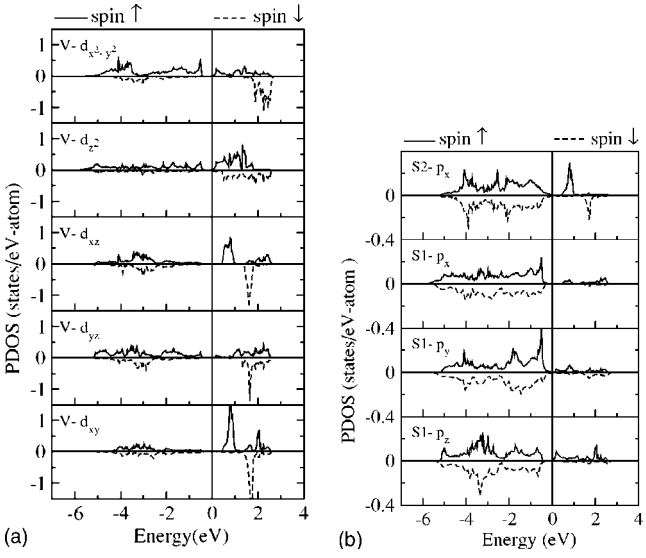


FIG. 6. PDOS of the AFM-C phase, projected over atomic sites and over *l* and *m* quantum numbers. The axis for the *m* decompositions are the same as Fig. 1, where *x* corresponds to the *a* axis, *y* to *b*, and *z* to the vertical direction *c*.

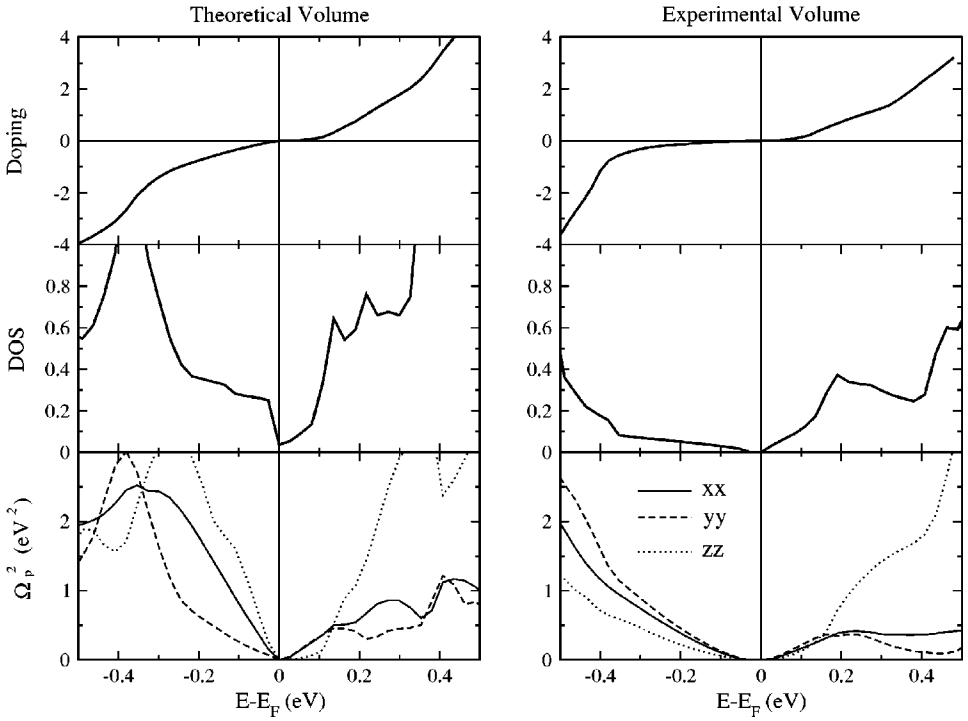


FIG. 7. Density of states around the Fermi level (in units of states/eV cell) and squared plasma frequencies (in $eV^2$) within a rigid band model given for both the equilibrium calculated volume (left panel) and the experimental one (right panel). The upper panels show the corresponding doping (in electrons).

gible near $E_F$. In the conduction region we find that the only states hybridized with V states are S2 $p_x$ orbitals. This is explained by the relatively short S2-V distance which is about 8% shorter than the S1-V one. The only states that contribute to the *A*-band are the S1 $p_y$ (50%) and S2 $p_x$ (50%) orbitals. The *B*-band mostly arises from the hybridization of V $d_{yz}$ (8%), $d_z^2$ (37%), and $d_{x^2-y^2}$ (16%) with $p_z$ (30%) S states. In the remaining energy interval ranging from −0.5 eV to −6 eV, we find an admixture of S and V *p* and *d* states. The large thickness of the lines in Fig. 4 reflects the fact that each f.u. contains three S atoms and only one V atom.

A further difference between the calculations performed at $V_{\text{th}}$ and at $V_{\text{expt}}$ is noted in Fig. 7. Here the details of the DOS and the squared plasma frequency, $\Omega_p^2$, are shown in the vicinity of $E_F$. The $\Omega_p^2$ calculations were carried out by assuming a rigid-band model. In the $V_{\text{expt}}$ case, the DOS is found to be zero at $E_F$ and remains negligible down to −0.4 eV. In the $V_{\text{th}}$ case, we found only a strong depletion at $E_F$ (0.036 states/eV) and a plateau of about 0.1 states/eV in the −0.4 eV $E_F$ region. The vanishing $N(E_F)$ at $V_{\text{expt}}$ leads to a vanishing $\Omega_p^2$ at $E_F$ and a large resistivity is expected at $T=0$. This behavior of $\Omega_p^2$ accounts for the experimental temperature dependence of $\rho(T)$ reported by Forró *et al.*,[16] who reported a very large resistivity in the $T=0$ limit at pressures below the critical pressure $p_{\text{cr}} \approx 2$ GPa needed to stabilize the metallic state.

In the upper panel of the same figure, we notice that hole doping would immediately increase the *A*-band hole pocket at Γ, thus enhancing the metallic character. This prediction is opposite to the experimental results. For example, the electrical resistivity is found to increase with decreasing temperature in sulfur-deficient samples with $\delta \approx 0.15$.[19] This discrepancy indicates that a rigid band approach is unsuitable to account for the effects of electron doping and a strong correlation approach should be used instead.

We conclude this section by briefly discussing the stability of the AFM-C in $BaVS_3$ in the context of the situation in cubic vanadium oxides where this phase is stabilized by orbital fluctation along the FM direction. The occurrence of a metal-insulator transition and subsequent stabilization of a long range AF order in the *ab*-plane explained by our *ab initio* calculations is compatible with a model of orbital ordering of the V 3*d* electron occupying the lowest-lying $t_{2g}$ quasidoublet, as proposed earlier.[40] Indeed, this ordering is associated with the octahedral/trigonal/orthorhombic crystal distortion at low temperature that stabilizes the structure and strongly renormalizes the anisotropic exchange energy *J* within a simple superexchange picture. A similar orbitally induced stabilization of an insulating AF phase is supported by both experimental evidence and theoretical arguments in vanadates like $V_2O_3$ (Ref. 41) or $LaVO_3$.[42] The analogy is compelling in spite of two major differences, (1) in $BaVS_3$, vanadium is tetravalent (S=1/2) and (2) the crystal-field splitting of the V 3*d* multiplet is also different owing to the reduced ionicity and larger distances of the V-S bonds as compared to vanadates. These differences should be considered in explaining the much higher $T_N = 140-150$ K of the vanadates.

### B. Pressure dependent properties

In this section we focus on the pressure-induced structural, magnetic, and electronic changes with emphasis on the MI transition. The effect of pressure was investigated by isotropically expanding and compressing the supercell of the AFM-C and FM magnetic phases along the three crystallographic directions. For each volume, we minimized the total energy by varying all atomic positions. However, to limit computational time, we kept the $c/a$ and $b/a$ ratio constant. The shrinking of the AFM-C cell is found to enhance the

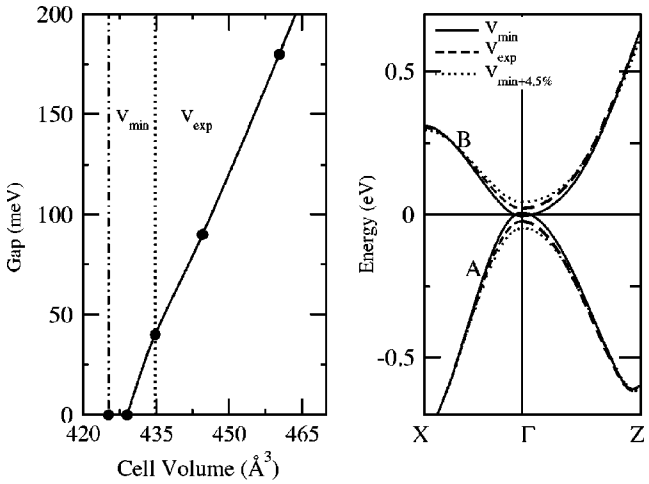


FIG. 8. (a) The dependence on cell volume of the energy gap. Compressions are performed increasing isotropically the cell parameters from the theoretical ones. (b) The two bands, called *A* and *B*, that flatten as the volume increases from the theoretical value reduces their overlap near Γ and causes a M-I transition.

metallic character; by enlarging the cell, the opposite occurs and a gap between occupied (*A*-band) and unoccupied states (*B*-band) is opened. In Fig. 8, we summarize this result by representing the value of the insulating gap as a function of volume and the pressure-dependent behavior of the *A* and *B* bands around $E_F$ along the $X-\Gamma$ and $\Gamma-Y$ directions. The trend in the whole Brillouin zone is not shown, since only the bands around $E_F$ differ significantly from those shown in Fig. 4. The two vertical lines in Fig. 8(a) indicate the minimum (dashed-dotted line) and the experimental (dotted line) volumes. The gap is opened for a volume of 429 Å$^3$ that corresponds to an expansion of 0.9% with respect to the equilibrium volume. The gap increases almost linearly with increasing pressure. Figure 8(b) shows that the major changes in the band structure occur in an ellipsoidal region around Γ, with semiaxes of 0.3 $(\pi/a, \pi/b, \pi/c)$. In this region, the MI transition takes place as a consequence of the splitting of the *A*- and *B*-bands.

We are now in the position to compare the pressure-induced changes on the metallic properties of the system by analyzing the trends of $\Omega_p^2(V_{\text{expt}})$ and $\Omega_p^2(V_{\text{th}})$ shown in Fig. 7. By recalling that the calculated equilibrium value of the cell volume, $V_{\text{th}}$, underestimates the experimental value $V_{\text{expt}}$, the results obtained at $V_{\text{th}}$ are equivalent to those obtained by compressing the crystal structure. An increase of $\Omega_p^2$ at $E_F$ is then expected. The overlap between the *A*- and *B*-bands increases upon pressure, thus we conclude that a larger conductivity and a metallic state are predicted at sufficiently high pressures, in agreement with the data by Forro *et al.*[16] In the pressure range of interest, the *A*- and *B*-bands exhibit an orbital decomposition similar to that calculated at ambient pressure. The only notable difference concerns the *B*-band, where a more pronounced S $p_z$ character (38%) is observed. In the remaining region of the Brillouin zone, the two bands almost overlap and no significant differences are found by varying pressure.

In the preceding paragraph, we have shown that the insulating gap increases with increasing cell volume (Fig. 8),

TABLE IV. Pressure effects on zigzag [$d_{\text{zigzag}}$(V-V), in Å], V-V distance (Å), and Δ (in meV).

| | $d_{\text{zigzag}}$(V-V) | $d_{\text{VV}}$ | Δ |
|---|---|---|---|
| $V_{\text{th}}$ | 0.242 | 2.856 | −12 |
| $V_{\text{th+2\%}}$ | 0.244 | 2.878 | 47 |
| $V_{\text{th+5\%}}$ | 0.248 | 2.900 | 92 |

regardless to the pressure-induced modifications of internal structural distortions (see Table IV). In the following, we show in detail how such distortions lead to qualitative changes of the ground state. For example, we previously noticed that pressure affects the S-V hybridization near $E_F$. We now concentrate on the role played by the zigzag displacement of the V chains and by the V-V (and S-V) distance. Indeed, these two quantities are sensitive to the change of lattice constants both along the *c*-direction and in the *ab*-plane (see Fig. 2). The V-V distance is modified either by changing the *c*-axis parameter or by increasing the V zigzag displacement. To study separately the two effects on the metal-insulator transition, we carried out two series of constrained calculations. In the first series we kept the cell dimensions fixed and modified the zigzag displacement. In the second one, the zigzag displacement was frozen at the theoretical value and the *c*-axis parameter was increased. The results are reported in Fig. 9, where the gap is plotted as a function of the V-V distance by keeping fixed either the volume [(A) circles] or the zigzag displacement [(B) triangles]. Although the V-V range for two cases is the same, the calculated gap values at a given V-V distance differ by one order of magnitude. A comparison between the two curves suggests that the V-V distance itself plays a marginal role and that the V zigzag displacement is rather the most relevant structural parameter governing the MI transition.

To further highlight the effect of the zigzag on the electronic structure of $BaVS_3$ we plot in Fig. 10 the band structure along *X*-Γ-*Z* for three different values of the zigzag: 0.24 Å, 0.11 Å, and 0. For the calculated case at equilibrium (zigzag=0.24 Å), the system is a poor metal, as already discussed. By decreasing the zigzag, the overlap between *A*- and *B*-bands increases. Finally, in the absence of zigzag, almost identical to the hexagonal phase, new bands cross $E_F$ and others appear below $E_F$. As a consequence, the DOS of the upper valence region is enhanced and a flattening of the DOS above $E_F$ is observed, differently from the DOS obtained for the quasimetallic calculated equilibrium structure shown in Fig. 5.

We conclude the discussion on the pressure effects by illustrating the effects on the stability of the AFM-C structure with respect to the FM one. The response of the former structure to the compression is a localization of the valence V 3*d* electrons. Accordingly, a variation of the total magnetic moment $\mu$ is observed and $\mu$ deviates from the equilibrium value $(1.30\mu_B)$ by $-0.08\mu_B$ for a 15% compression with respect to the equilibrium volume. The corresponding variations of magnetic moment at the S1 and S2 sites is $0.03\mu_B$. In the case of the FM structure, the magnetic moment remains nearly unchanged for small compression values up to

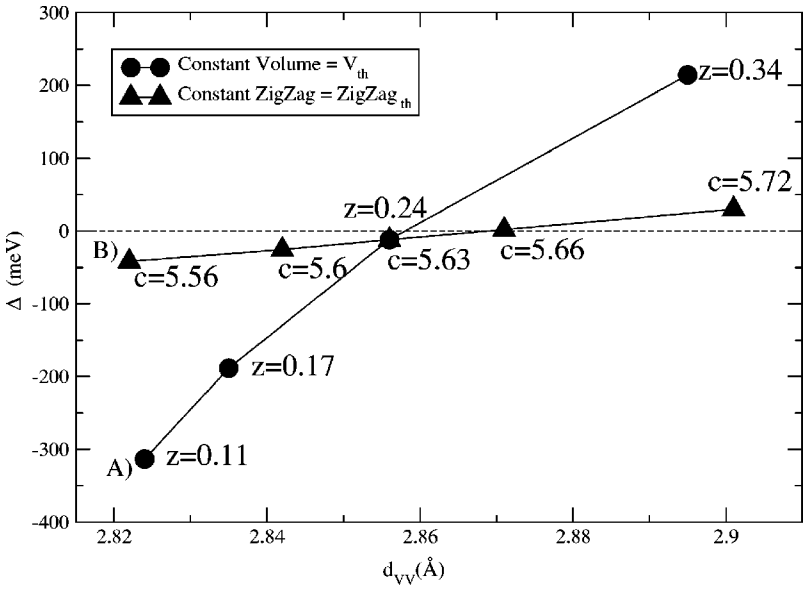


FIG. 9. Values of the gap with respect to the V-V distance for two different constrained calculations: at fixed volume [(A) circles] and at a fixed zigzag [(B) triangles]. The lines are guides for the eyes. The values of the zigzag ($z$) and of the $c$ cell parameter are also given for $A$ and $B$, respectively.

8% and decreases by less than $0.03\mu_B$ for a 15% compression. The different response of the FM and AFM-C structures explains the crossover of phase stability predicted at $V=0.83V_{\text{th}}$ (see Fig. 11). Below this volume value, the FM structure is favored and the new value of the exchange integral $J_2$ is 12.9 meV. As compared to the ambient pressure case, where $J_2=-1.1$ meV, the sign changes and the absolute value is enhanced by one order of magnitude. The latter effect is ascribed to the change of interchain distance that decreases from 6.72 Å at $V=V_{\text{th}}$ to 6.3 Å. This increases the exchange interaction between SNN V atoms. The above pressure-induced crossover from AFM-C to FM predicted by our calculations is supported by the experimental data by Gauzzi *et al.*[11] on partially Sr-doped samples, where the Sr-induced chemical pressure was found to induce the crossover for 10% substitution level.

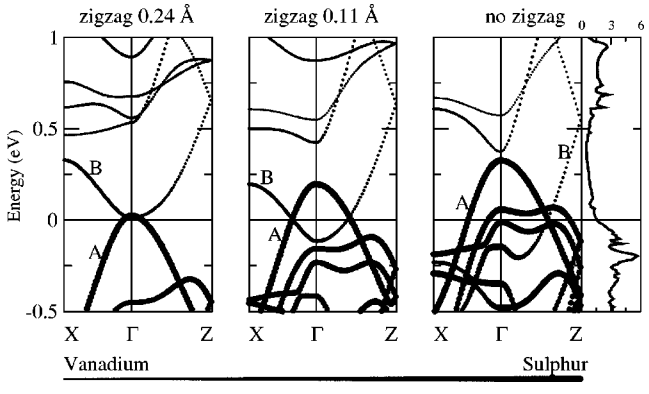


FIG. 10. Here we report the effect of changing the V displacement, keeping fixed the theoretical Bravais lattice for orthorhombic $BaVS_3$. As the zigzag passes from the theoretical value of 0.24 Å to the value of 0.11 Å, the overlap between $A$ and $B$ increases strongly and other bands approach $E_F$ from down. When the zigzag is set to zero, $B$ shows a complete hybridization in the $X\Gamma$ direction and a third band crosses the Fermi level. For zigzag=0 the total DOS are also shown.

## VI. SUMMARY

In conclusion, we reported electronic structure calculations on the hexagonal perovskite $BaVS_3$ within the LSD and the LSD+$U$ approximations. The structural and electronic properties of the ground state have been studied in detail for different possible magnetic structures. We found that the LSDA+$U$ is suitable to account for the salient features. Notable is the agreement within 1–2 % between calculated and measured lattice parameters and atomic positions. Agreement is also found regarding the insulating and AFM-C character of the ground state, while the Nèel transition temperature was overestimated as discussed in detail in Sec. V A.

We also investigated in detail the pressure-induced changes on the electronic and magnetic properties of $BaVS_3$

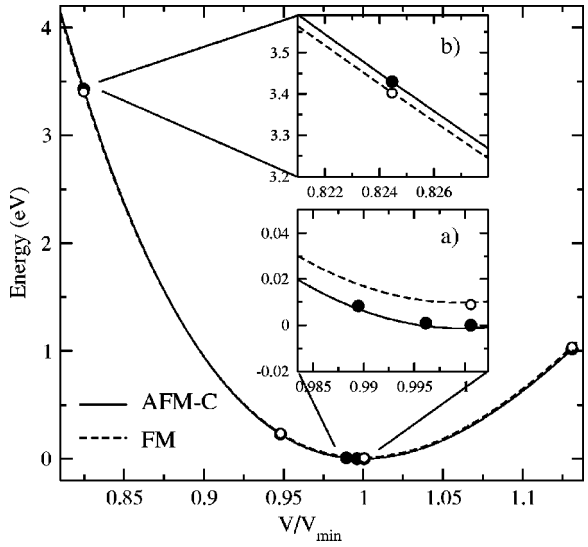


FIG. 11. Energy/volume curves for the AFM-C (–●–)and FM (- -○- -) systems. The two phases are nearly degenerate at the point of minimum energy, and for a compression of about 15% of cell volume we calculated a crossing between the two curves. The two zooms mark the change in relative stability.

by minimizing the total energy as a function of atomic positions for different cell volumes. We found that a volume expansion of about 1% leads to a MI transition with a small gap of 47 meV, in agreement with the experimental value of 43–59 meV. The most relevant structural parameter to the MI transition was found to be the transversal zigzag displacements of the V atoms forming V-V chains along the *c*-axis. Finally, a 15% volume compression was found to induce a crossover from the AFM-C phase to the FM phase, also in full agreement with experimental data on partially Sr-substituted where the Sr-induced chemical pressure was found to induce the crossover for 10% substitution level.

In order to understand the rich electronic and magnetic structure of $BaVS_3$ revealed in experiments, further theoretical efforts, such as the analysis of chemical substitutions (Ba→Sr, V→Ti, and S deficiencies) and orbital ordering, would be of great interest. We also believe that the nature of the short range in-plane correlations characterizing the nonmagnetic insulating phase observed between 70 K and 30 K, a central issue of debate, probably hard to explain within the LDA+$U$ scheme, deserves further investigations, both theoretical and experimental.

## ACKNOWLEDGMENTS

The authors acknowledge N. Barisic, P. Fazekas, L. Forro, E. Gilioli, F. Licci, and M. Marezio for useful discussions. This work was partially supported by a supercomputing grant at Cineca (Bologna, Italy) through the Istituto Nazionale di Fisica della Materia (INFM). The authors also thank the Technical University of Vienna for the use of computer time.

*Also at INFM–LAMIA, Laboratory of Innovative and Artificial Materials, Corso Perrone 24, I-16152 Genova Italy.

[1] A. M. Oleś, M. Cuoco, and N. B. Perkins, in *Lectures on the Physics of Highly Correlated Electron Systems IV*, edited by F. Mancini, AIP Conf. Proc. No. 527 (AIP, Melville, NY, 2000), pp. 226–380.
[2] M. Imada, A. Fujimori, and Y. Tokura, Rev. Mod. Phys. **70**, 1039 (1998).
[3] S.-W. Cheong and H. Y. Hwang, in *Colossal Magnetoresistive Oxides*, edited by Y. Tokura (Gordon and Breach, Tokyo, 1999).
[4] R. A. Gardner, M. Vlasse, and A. Wold, Acta Crystallogr., Sect. B: Struct. Crystallogr. Cryst. Chem. **25**, 781 (1969).
[5] G. Mihály, I. Kézsmárki, F. Zámborszky, M. Miljak, K. Penc, P. Fazekas, H. Berger, and L. Forró, Phys. Rev. B **61**, R7831 (2000).
[6] L. F. Mattheiss, Solid State Commun. **93**, 791 (1995).
[7] M. Takano, H. Kosugi, N. Nakanishi, M. Shimada, T. Wada, and M. Koizumi, J. Phys. Soc. Jpn. **43**, 1101 (1977).
[8] M. Ghedira, J. Chenavas, F. Sayetat, and M. Marezio, Acta Crystallogr., Sect. B: Struct. Crystallogr. Cryst. Chem. **37**, 1491 (1981).
[9] M. Ghedira, M. Anne, J. Chenavas, M. Marezio, and F. Sayetat, J. Phys. C **19**, 6489 (1986).
[10] M. Nakamura, A. Sekiyama, H. Namatame, A. Fujimori, H. Yoshihara, T. Ohtani, A. Misu, and M. Takano, Phys. Rev. B **49**, 16 191 (1994).
[11] A. Gauzzi, F. Licci, N. Barišić, G. L. Calestani, F. Bolzoni, E. Gilioli, M. Marezio, A. Sanna, C. Franchini, and L. Forró, Int. J. Mod. Phys. B **17**, 3503 (2003).
[12] T. Graf, D. Mandrus, J. M. Lawrence, J. D. Thompson, P. C. Canfield, S. W. Cheong, and L. W. Rupp, Phys. Rev. B **51**, 2037 (1995).
[13] H. Imai, H. Wada, and M. Shiga, J. Phys. Soc. Jpn. **65**, 3460 (1996).
[14] H. Nakamura, H. Imai, and M. Shiga, Phys. Rev. Lett. **79**, 3779 (1997).
[15] C. H. Booth, E. Figueroa, J. M. Lawrence, M. F. Hundley, and J. D. Thompson, Phys. Rev. B **60**, 14 852 (1999).
[16] L. Forró, R. Gaál, H. Berger, P. Fazekas, K. Penc, I. Kézsmárki, and G. Mihály, Phys. Rev. Lett. **85**, 1938 (2000).
[17] I. Kézsmárki, Sz. Csonka, H. Berger, L. Forró, P. Fazekas, and G. Mihály, Phys. Rev. B **63**, 081106 (2001).
[18] M. Shiga, H. Imai, H. Mitamura, and T. Goto, Physica B **294–295**, 149 (2001).
[19] T. Yamasaki, H. Nakamura, and M. Shiga, J. Phys. Soc. Jpn. **69**, 3068 (2000).
[20] H. Nakamura, T. Yamasaki, S. Giri, H. Imai, M. Shiga, K. Koijma, M. Nishi, K. Kakurai, and N. Metoki, J. Phys. Soc. Jpn. **69**, 2763 (2000).
[21] Z. V. Popović, G. Mihály, I. Kézsmárki, H. Berger, L. Forró, and V. V. Moshchalkov, Phys. Rev. B **65**, 132301 (2002).
[22] T. Inami, K. Ohwada, H. Kimura, M. Watanabe, Y. Noda, H. Nakamura, T. Yamasaki, M. Shiga, N. Ikeda, and Y. Murakami, Phys. Rev. B **66**, 073108 (2002).
[23] W. Higemoto, A. Koda, G. Maruta, K. Nishiyama, H. Nakamura, S. Giri, and M. Shiga, J. Phys. Soc. Jpn. **71**, 2361 (2002).
[24] P. Fazekas, K. Penc, H. Berger, L. Forró, Sz. Csonka, I. Kézsmárki, and G. Mihály, Physica B **312–313**, 694 (2002).
[25] I. Kézsmárki, G. Mihály, R. Gaál, N. Barišić, H. Berger, L. Forró, C. C. Homes, and L. Mihály, cond-mat/0311335 (unpublished).
[26] S. Fagot, P. Foury–Leylekian, S. Ravy, J. P. Pouget, and H. Berger, Phys. Rev. Lett. **90**, 196401 (2003).
[27] H. Nakamura, H. Tanahashi, H. Imai, M. Shiga, K. Koijma, K. Kakurai, and M. Nishi, J. Phys. Chem. Solids **60**, 1137 (1999).
[28] M. H. Whangbo, H. J. Koo, D. Dai, and A. Villesuzanne, J. Solid State Chem. **165**, 345 (2002).
[29] O. Massenet, R. Buder, J. J. Since, C. Schlenker, J. Mercier, J. Kebler, and D. G. Stucky, Mater. Res. Bull. **13**, 187 (1978).
[30] G. Kresse and J. Furthmüller, Phys. Rev. B **54**, 11 169 (1996).
[31] J. P. Perdew and A. Zunger, Phys. Rev. B **23**, 5048 (1981).
[32] M. Imada, A. Fujimori, and Y. Tokura, Rev. Mod. Phys. **70**, 1039 (1998).
[33] V. I. Anisimov, J. Zaanen, and O. K. Andersen, Phys. Rev. B **44**, 943 (1991).
[34] S. L. Dudarev, G. A. Botton, S. Y. Savrasov, C. J. Humphreys, and A. P. Sutton, Phys. Rev. B **57**, 1505 (1998).
[35] T. Mizokawa and A. Fujimori, Phys. Rev. B **54**, 5368 (1996).
[36] Z. Yang, Z. Huang, L. Ye, and X. Xie, Phys. Rev. B **60**, 15 674

(1999).
[37] P. E. Blöchl, Phys. Rev. B **50**, 17 953 (1994).
[38] G. Kresse and D. Joubert, Phys. Rev. B **59**, 1758 (1999).
[39] J. S. Smart, Phys. Chem. Solids **11**, 97 (1959). Some of the authors have already described the details of the calculation of exchange parameters and Néel temperature in N. Lampis, C. Franchini, G. Satta, A. Geddo-Lehmann, and S. Massidda, Phys. Rev. B **69**, 064412 (2004).
[40] G. Mihály, I. Kézsmárki, F. Zámborszky, M. Miljak, K. Penc, P. Fazekas, H. Berger, and L. Forró, Phys. Rev. B **61**, R7831 (2000).
[41] L. Paolasini, C. Vettier, F. de Bergevin, F. Yakhou, D. Mannix, A. Stunault, W. Neubeck, M. Altarelli, M. Fabrizio, P. A. Metcalf, and J. M. Honig, Phys. Rev. Lett. **82**, 4719 (1999).
[42] G. Khaliullin, P. Horsch, and A. M. Oleś, Phys. Rev. Lett. **86**, 3879 (2001).